How dynamics changes ammonia cracking on iron surfaces

Simone Perego,[1,2] Luigi Bonati,[1] Shivam Tripathi,[3] and Michele Parrinello[1,a)]

[1)] *Atomistic Simulations, Italian Institute of Technology, 16156 Genova, Italy*

[2)] *Department of Materials Science, Università di Milano-Bicocca, 20126 Milano, Italy*

[3)] *Department of Materials Science and Engineering, Indian Institute of Technology Kanpur, Uttar Pradesh, India*

Ammonia is a promising hydrogen carrier, being rich in hydrogen and ease of transport. However, a microscopic characterization of the ammonia cracking reaction is still lacking, hindered by extreme *operando* conditions. Leveraging state-of-the-art molecular dynamics, machine learning potentials, and enhanced sampling methods, we offer an atomistic view of the adsorption, diffusion, and dehydrogenation processes of NH_x ($x = 1, 3$) on two representative surfaces at *operando* temperature of 700 K. Dynamics pervasively affects all steps of decomposition, including on the stable (110) surface where the high mobility of reaction intermediates affects the reactivity. The role is even more dramatic on the (111) surface, where the mobility of Fe surface atoms introduces new adsorption sites and alters the dehydrogenation barriers. In both cases, a detailed analysis of reactive events shows that there is never a single transition state, but it is always an ensemble composed of at least two pathways. Notwithstanding, a unified mechanism can be identified by following the charge transfer along the different reaction pathways.

I. INTRODUCTION

The urgent need to move towards a green economy has spurred growing interest in the potential use of ammonia as a hydrogen vector[1]. Ammonia has a significant weight fraction of hydrogen and, coupled with its practical advantages such as the moderately low temperature at which it liquefies of -33 °C at atmospheric pressure, offers a significant advantage over molecular hydrogen (H_2) in terms of ease of transport and storage[2,3]. The attractivity of hydrogen production from ammonia relies on its potential for on-site and on-demand generation[4]. However, the successful implementation of this step necessitates the development of efficient methodologies for extracting hydrogen from ammonia.

Thermal decomposition, or catalytic cracking, stands as the predominant technique for hydrogen generation from ammonia[4]. Having in mind industrial applications, most of the attention has been concentrated on non-noble metals like Fe, Co, and Ni and their alloys[5]. In the following, we focus on iron, which is a prototypical thermocatalyst in both the Haber-Bosch process and its inverse. These reactions are known to be highly structure-sensitive, with Fe(110) and Fe(111) representing two limiting cases among the low-index surfaces. In fact, the former is characterized by high density and stability but low catalytic activity, while the latter has an open structure and high activity[6,7].

Unfortunately, in spite of more than a century of efforts, a comprehensive characterization of both processes remains elusive due to extreme *operando* conditions which make experiments and simulations challenging. Indeed, the operational temperatures for catalytic cracking on iron at 1 atm lie in the range of 400-750 °C[4]. Experimental information about the reaction intermediates has thus been obtained in conditions far from the *operando* regimes[8,9], or extrapolated through indirect temporal analysis of products (TAP) measurements[10]. Notably, a high surface sensitivity has been reported[8,9], similarly to what was observed in the synthesis process[7,11]. Only very recently, direct *operando* probing of synthesis reaction intermediates have been performed[12], confirming the structure sensitivity and showing nontrivial temperature dependency in the rate-limiting step.

From a computational perspective, there is a large number of theoretical studies on ammonia decomposition based on T=0 K density functional theory (DFT) calculations[10,13–22]. However, these studies do not fully consider the influence of dynamics, which is of paramount importance in industrial catalysts[23,24]. This crucial role is clearly emerging in recent simulations[25–33]. In particular, in the case of ammonia decomposition, Gerrits and Kroes have highlighted the role of dynamics on the Ru(0001) surface through *ab initio* molecular dynamics (AIMD) simulations[28].

Molecular dynamics (MD) represents an ideal tool to investigate the system dynamics, as it acts as a computational microscope with atomic resolution over multiple time scales[26,30]. It can also operate effectively at high temperatures without the practical constraints that *in operando* experiments have. However, the high computational cost of DFT calculations limits the time-scales and system sizes that can be simulated. Recent methodological advances in machine learning (ML)-based interatomic potentials and state-of-the-art enhanced sampling techniques allowed lifting these limitations and elucidating the mechanistic details of reactive processes since long-timescales and large system-size simulations have been made accessible[32,34–38]. Of particular relevance here are the recent investigations of the dissociative chemisorption of N_2 on the Fe(111) surface[32,33], where these techniques have allowed the dramatic role that dynamics could play at *operando* temperatures to be uncovered. Indeed, the diffusion of surface atoms results in the continuous creation

[a)] michele.parrinello@iit.it

and destruction of active sites, highlighting the dynamic nature of the catalytic process[32] in line with the earlier hypothesis. The effect of dynamics becomes even more striking when we also account for lateral interactions[33].

In this manuscript, we apply the methodology earlier developed[32] to investigate the adsorption, diffusion, and deprotonation of nitrogen hydrides (NH_x, x=1-3) at the *operando* temperature of T=700 K on both the Fe(111) and Fe(110) surfaces. We provide a comprehensive statistical and chemical characterization of these processes on the highly dynamic iron surfaces. An indispensable tool in the characterization of these processes is our ability to monitor the electronic charge distribution at modest computational effort also in large systems. This ability allows the adsorption environments and the progress of the reaction under evolving surface conditions to be followed. We find that, like in the case of the ammonia formations, the two surfaces behave rather differently. In the more rigid Fe(110) case, the low and high temperatures are similar, and an Arrhenius-type behavior is observed. In contrast, the highly dynamical behavior of the less dense Fe(111) leads to the formation of new adsorption sites and results in a non-Arrhenius behavior.

However, in spite of the different behavior that manifests itself in a variety of transition states and reaction pathways, a unified description can still be obtained. Furthermore, we establish a correlation between diffusion and dehydrogenation free energy barriers, underscoring once again the role of dynamics in heterogeneous catalysis.

II. METHODS

A. Constructing an *ab initio*-quality potential

To accurately describe reactive simulations in which chemical bonds can be formed and broken, an accurate description of the electronic states as the system evolves is mandatory. This could be obtained using AIMD. However, its high computational cost hinders its application to realistic systems where large-scale structures have to be simulated over extended timeframes, such as nanoseconds and beyond. Since the pioneering work of Behler and Parrinello[39], ML-based potentials have emerged as a viable solution to bridge the gap between the accuracy offered by DFT-based methods and the computational efficiency of semiempirical force fields[40]. By fitting the energy and forces as a function of the atomic positions on a dataset of DFT calculations, these potentials can provide an *ab initio*-like accuracy at a tiny fraction of the cost. However, for this procedure to be successful, all the thermodynamically relevant configurations need to be included in the training set. In the study of catalytic activity, it is particularly critical to include reactive configurations for all steps of interest.

Since collecting all these reactive configurations through AIMD simulations can be prohibitively expensive, we iteratively construct the reference database via an active learning strategy. In each iteration, we use the machine learning potential to sample new configurations through MD simulations (the first one is fitted only on AIMD data). Then, a subset of these structures is selected, and single-point DFT calculations are performed. These data are then incorporated into the training set to optimize a new potential, which will be used to sample new configurations. One way to identify structures that are not adequately described by the potential is to use a *query-by-committee* approach, in which the standard deviation of the predictions of a set of models is used as a proxy for the uncertainty. The usage of advanced sampling methods, the same that we use later for studying the catalytic reactivity (see Section II C 1), enhances this active learning procedure. Indeed, it allows us to harvest uncorrelated structures and especially reactive ones. Moreover, since it has been shown that the query-by-committee selection criterion does not always adequately describe all reactive pathways, being unbalanced on reactants and products[36], we added more configurations belonging to the transition state region. This procedure (sampling, selection and DFT single point, training) is iterated until a reliable potential for describing the full reactive pathways is obtained.

The resulting dataset comprises about 110K configurations, the detailed composition of which is given in the Supplementary Information (SI) Tables S I, S II. These include some of the calculations we collected for the ammonia synthesis studies on Fe[32,33], along with many others made specifically for this work to ensure that all of the following physical scenarios of interest were considered:

- long-term dynamics of Fe surfaces
- surface with nitrogen hydrides (NH_x, where x ranges from 3 to 1)
- diffusing hydrides
- reactive configurations of all dehydrogenation steps.

1. ML-based potential details

To fit the potential energy we employed the Deep Potential Molecular Dynamics (DeepMD)[41,42] method. Here, we report the technical details. Three hidden layers with [30, 60, 120]/[240, 240, 240] nodes per each were used respectively for the embedding and fitting network. A cutoff radius of 6.0 Å (with 0.3 Å switching function for continuity) was set for interacting atoms. In the training phase, an exponential-type learning curve was applied to decrease the learning rate from 0.001 to 3.5×10^{-8}. The decay step was set to 2 epochs, and the models were trained for 200 decay steps. The performance was evaluated on energy and forces with a weighted root mean square error (RMSE) loss function. The weights of the energy and forces were adjusted during the optimization from 0.02 to 1, and from 1000 to 1, respectively. In the active learning procedure, an ensemble of 4 different models is optimized in parallel on permutations of

the training and validation datasets to assign an uncertainty to the configurations. At the end of the active learning procedure, the achieved RMSE for energy and forces are 1meV/atom and 50meV/A, respectively (see SI, Figure S1)

2. Reliability of ML-based potential

Furthermore, to benchmark the reliability of the potential, we used it to calculate the potential energy barriers for all dehydrogenation steps. The dimer method was used to identify the transition states[43,44]. A $4 \times 6 \times 5$ Fe(110) slab (120 atoms) and a $4 \times 4 \times 6$ Fe(111) slab (96 atoms) along with an NH_x (x=1-3) molecule were implied at this stage. Geometries were optimized using a force-based conjugate gradient method in all calculations. The lowest two and three Fe layers were kept fixed during optimization and MD calculations for (110) and (111) surfaces, respectively. Saddle points and minima were considered convergent when the maximum force in each degree of freedom was less than 0.01 eVÅ^{-1}. So, we recalculated the energy difference between the structures obtained at the DFT level. SI Table S III shows the achieved results. The activation energies are in excellent agreement with a maximum discrepancy of 0.07 eV.

3. DFT calculations

All the AIMD simulations, as well as single point DFT calculations used to build the reference database, were performed using the PWscf code of Quantum ESPRESSO (QE)[45–47]. Exchange-correlation effects have been treated within the generalized-gradient approximation with the Perdew-Burke-Ernzerhof (PBE) functional[48]. We employed ultrasoft RRKJ pseudopotentials[49] along with plane-wave basis with a 640 and 80 Ry cutoff for wavefunction kinetic energy and charge density, respectively. The Marzari-Vanderbilt cold smearing technique[50] with a Gaussian spreading of 0.04 Ry was used to treat the state occupations. Spin polarization was included to describe the magnetic properties of iron properly. The lowest Fe layers were kept fixed during optimization and MD calculations for (100) and (110) surfaces, while the lowest twos were for the (111) and (211) surfaces. A vacuum layer of at least 10 Å was included in the z-direction of all the slab models to prevent self-interaction effect. The Brillouin zone was sampled using a $2 \times 2 \times 1$ Monkhorst-Pack k-point grid[51].

AIMD simulations were performed in a constant volume and temperature (NVT) ensemble using the stochastic velocity rescaling thermostat[52] with a time step of 1.0 fs at temperatures ranging from 600 to 800 K. In addition, enhanced sampling simulations (see Section II C 1) were performed to simulate the reactive events and to explore a broader configurational space.

4. Machine learning for partial charges

A key property that we monitor to understand the activity of the catalyst is the amount of charge transferred during the adsorption and the dehydrogenation step. Following the same methodology developed in Ref. 32, we trained a second neural network to predict partial charges based on the atomic positions and chemical species. Reference values are obtained from a subset of the dataset used for the potential (comprised of ≈75,000 structures), using the Bader charge decomposition scheme[53,54]. Since partial charges are *per atom* property, the NN can be trained on small systems and used to predict the charge for arbitrarily large systems.

To train the NN we used the deep tensor neural network SchNet[55] architecture, using the same parameters as in Ref. 32: 5 interaction layers, pairwise distances expanded on 30 Gaussians and 64 atom-wise features, 3.5 Å cosine cutoff, atom-wise module with 2 hidden layers and [64, 64] nodes per layer. To optimize the parameters, we use the RMSE between the predicted charges $\{q_i\}$ and the reference ones $\{q_i^{DFT}\}$ as loss function:

$$L = \frac{1}{N_{at}} \sum_i (q_i - q_i^{DFT})^2 \tag{1}$$

The dataset is split in training/validation subsets with a ratio of 80:20, and the model is trained using the ADAM optimizer[56] with a learning rate of 0.001 and the early stopping criterion. With these parameters, the model achieved an RMSE on the validation set of 10^{-4} e.

We then express the charge transferred between atoms as the deviation from their nominal valence charge q^v ($8e$, $5e$, $1e$ for Fe, N, and H, respectively). The total charge transferred from the metallic substrate to the NH_x species can be computed as $q_{NH_x} = \sum_{i \in NH_x} (q_i - q_i^v)$.

B. Molecular dynamics simulations

Classical molecular dynamics simulations were performed using the Large-scale Atomic/Molecular Massively Parallel Simulator (LAMMPS) software[57], supplemented by DeepMD-kit 2.1[58] and PLUMED[59]. The time step was set to 0.5 fs, and the temperature was controlled with a stochastic velocity scaling thermostat[52] with a coupling constant of 100 fs.

Small surfaces containing 40 to 108 Fe atoms and up to 10 adsorbates (N/H) were simulated during the active learning phase.

After having optimized the potential, longer simulations of at least 20 ns were performed using an $8 \times 10 \times 10$ Fe(110) slab (800 atoms) along with an NH_x (x=1-3) molecule to simulate adsorption and dissociation. Analogously, an $8 \times 8 \times 12$ Fe(111) slab (768 atoms) along with an NH_x (x=1-3) molecule were simulated. For the (110) and (111) slabs, two and three layers of the slab were fixed to create a boundary condition that imitates that of a semi-infinite

slab. Periodic boundary conditions were utilized in the x- and y-directions, while a reflecting wall was implemented over the surface in the z-direction. The distance between the wall and the top layer varied with temperature to maintain a partial pressure of NH_3 equal to 1 bar, based on the ideal gas equation of state.

C. Free energy calculations

1. Enhanced sampling methods

Despite the existence of ML-based potentials, numerous reactive processes, such as chemical reactions, unfold over timescales that surpass the limits of conventional simulations. Consequently, a spectrum of advanced sampling methods has been devised to facilitate the simulation of rare events, addressing the challenge posed by these extended timescales. In this work, we used the collective variables(CVs)-based method On-the-fly Probability Enhanced Sampling (OPES)[60,61], implemented in the open-source PLUMED plugin[59,62]. CVs are analytical functions of atomic coordinates R that are purposely chosen to represent hard-to-sample modes and to distinguish between the metastable states. In OPES, a time-dependent external bias $V(s(R))$ is added to the interacting potential $U(R)$ in order to amplify the fluctuation of the CVs. During the simulation, the bias is adjusted according to the equilibrium probability distribution $P(s)$ in order to sample a predetermined target distribution $P^{tg}(s)$ as follows:

$$V(s) = -\frac{1}{\beta} log \frac{P^{tg}(s)}{P(s)} \ , \tag{2}$$

where β is the inverse thermodynamic temperature. At convergence, the $P(s)$ tends to the P^{tg}(s). Here, we assign the well-tempered distribution as the target, where $P^{tg}(s) \propto P(s)^{\frac{1}{\gamma}}$. By choosing appropriately a value of $\gamma = \beta\Delta E > 1$ the equilibrium distribution is broadened and the free energy barriers are lowered by a bias factor γ.

2. Free energy surface

The free energy surface (FES) along a set of collective variables is defined as the logarithm of their marginal probability $P(s)$:

$$F(s) = -\frac{1}{\beta} \log P(s). \tag{3}$$

An unbiased estimate of the probability density can be obtained from an OPES simulation via a simple reweighting scheme[60]:

$$P(s) = \frac{\langle \delta(s - s(R)) e^{\beta V(s(R))} \rangle_V}{\langle e^{\beta V(s(R))} \rangle_V} \tag{4}$$

which is valid when the bias has reached a quasi-static regime. To derive $P(s)$ from discrete simulation data, we utilize a weighted Gaussian density estimator. The weights in this estimator are determined by $w_t = e^{-\beta V(s_t)}$.

In order to compute the minimum free energy pathways from the two-dimensional FES, we utilized the Minimum Energy Path Surface Analysis (MEPSA) package[63].

3. Collective variables

An appropriate choice of the CVs to be biased allows us to focus the sampling on the process of interest. Different CV sets have been used for the different processes studied here (adsorption, diffusion, and dehydrogenation).

An important CV used for both enhancing sampling and analysis is the coordination number between the nitrogen atom and iron/hydrogen atoms, computed in differentiable form as:

$$C_{N,X} = \sum_{i \in X} s(r_i) \, , \qquad s(r_i) = \frac{1 - (\frac{r_i - d_0}{r_0})^n}{1 - (\frac{r_i - d_0}{r_0})^m} \tag{5}$$

where r_i is the distance between the N atom and the i-th atoms of X specie, r_0, d_0, n, and m, are tunable parameters. When used as a CV with OPES, the parameters are set as follows: $r_0 = 3.0\,(0.8)$ Å, $d_0 = 0.0\,(0.7)$ Å, $n = 6\,(5)$, and $m = 10\,(7)$ for $C_{N,Fe}\,(C_{N,H})$. In the analysis context, the following set of parameters is adopted for the $C_{N,Fe}$: $r_0 = 1.5$ Å, $d_0 = 1.0$ Å, $n = 6$, and $m = 12$. This latter choice allows us to identify a sharper coordination number related to the only first neighborhood shell. Analogously, for inspecting the dehydrogenation events and their transition state (see Section II C 4), we define the coordination between the reactive H and Fe atoms $C_{H,Fe}$ with the following parameter: $r_0 = 1.5$ Å, $d_0 = 0.5$ Å, $n = 6$, and $m = 12$.

To study the diffusion on NH over Fe(110), we use as CVs the position on the plane of the center of mass of the molecule expressed in terms of the lattice vector direction:

$$v_{1\bar{1}1} = \frac{1}{a\sqrt{3}\cos\alpha\sin\alpha}(x\sin\alpha + y\cos\alpha) \tag{6}$$

$$v_{1\bar{1}\bar{1}} = \frac{1}{a\sqrt{3}\cos\alpha\sin\alpha}(-x\sin\alpha + y\cos\alpha) \tag{7}$$

where x and y are the coordinates of the center of mass along the [001] and [1$\bar{1}$0] directions, α is the angle between [1$\bar{1}$1] and [1$\bar{1}$0] directions, and a is the lattice parameter. We set OPES barrier parameter ΔE equal to 40 kJ mol^{-1} and the OPES bias was updated every 500 steps. Harmonic restraints with an elastic constant of 10000 kJ mol^{-1}were applied on both the two CVs when $|v| \geq 1.6$. In such a way, we restrict the number of accessible metastable states without reducing the size of the supercell. The same restraints were applied to study the diffusion of NH_3 and NH_2, while no biases were applied due to the small diffusion barriers.

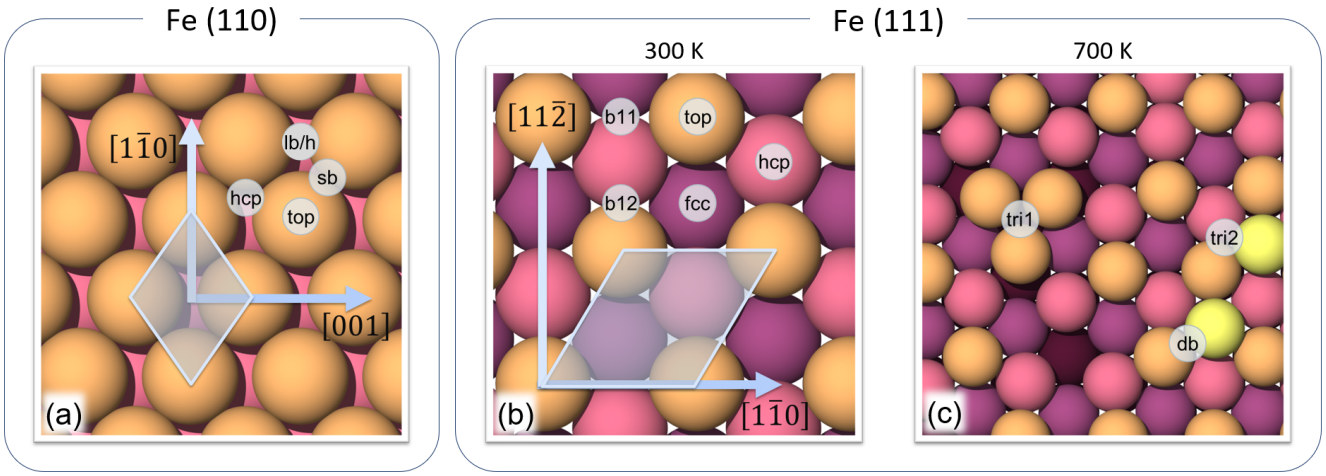

Figure 1. **Adsorption Sites.** Top view of Fe(110) (a) at 700K, Fe(111) at 300K (b) and 700K (c). Frames are captured from unbiased simulations where the atomic positions are 10 ps averaged to suppress the thermal fluctuations. Iron atoms are colored by layer. Gray-shaded areas mark the primitive unit cell. White-gray labeled circles are used to denote high-symmetry adsorption sites. (a) For Fe(110): sb, short-bridge; lb, long-bridge; h, hollow. (b) For ideal Fe(111): b11, bridge between top-layer atoms; b12, bridge between first and second layer. (c) For high-temperature Fe(111), we highlight the formation of new adsorption sites due to the surface roughness: tri1, triangular reconstruction; tri2, high symmetry site between three consequential layers; db, defective b12. These two last sites exist only on the defective surface due to the absence of b11 site

To simulate the first dehydrogenation step we use a set of 3 CVs: the $C_{N,Fe}$, the $C_{N,H}$, and a geometrical CV based on the angular distribution function defined as follows:

$$\Theta = \int_{\alpha}^{\beta} \sum_{ij \in H} s(r_i)s(r_j) \frac{1}{\sqrt{2\pi}w} \exp\left(-\frac{(\theta - \theta_{ij})^2}{2w^2}\right) \quad (8)$$

Where θ_{ij} are the HNH angles, r are the NH distances, $\alpha = 0.55\pi$, $\beta = 0.65\pi$, and $w = 0.5(\alpha - \beta)$. The OPES barrier parameter was set at 60 (80) kJ mol^{-1} for the 110 (111) surface and the OPES bias was updated every 1000 steps. A harmonic restraint was applied when $C_{N,H} \leq 2.5$, utilizing an elastic constant of 2000 kJ mol^{-1}. This restraint, which acts immediately after the dehydrogenation occurs, is aimed at facilitating reversible sampling eliminating the need to wait for hydrogenation to take place.

For the following dehydrogenation steps, we use as biased CVs the $C_{N,Fe}$, and the $C_{N,H}$ coordination numbers. The OPES barrier parameter was set at 40 (90) kJ mol^{-1}and 80 (50) kJ mol^{-1}for the second and third dehydrogenation steps over the 110 (111) surface, respectively. The bias was updated every 1000 steps in all the simulations and a harmonic restraint with an elastic constant of 2000 kJ mol^{-1}was applied when $C_{N,H} \leq 1.5$ or $C_{N,H} \leq 0.5$.

4. *Transition states characterization*

To obtain an unbiased characterization of the transition states (TS), no bias potential should be added in this region[64,65]. To this end, we perform an additional set of simulations of each dehydrogenation step in the OPES-flooding scheme described in[66]. Briefly, in this method, the OPES barrier parameter ΔE is properly chosen to a value lower than the effective barrier, and the transition state region is excluded from any bias potential modifications. In such a way, dehydrogenation events are observed to be bias-free. These simulations enable us to collect statistics on the reactive pathways and characterize the TS ensemble without any prior assumptions about the location of the transition and final states.

The same CVs of the standard OPES simulations are applied to describe each dehydrogenation step, but with lower barrier parameters and no elastic constraints applied. The OPES barrier parameters ΔE are set equal to 50(60), 20(65), and 65(50) kJmol^{-1}for each step respectively, while no bias is added in the region where $C_{N,H}$ is lower than 2.82,1.85,0.9.

One hundred simulations of dehydrogenation events were performed for each step and surface. We then defined the TS as the configuration in which the bonding distance between the N atom and the reactive H atom, $d_{N,H}$, is closest to 1.40 Å. This definition coincides with the maximum free energy of the dehydrogenation barrier (see SI, Figure S4). To characterize the TS ensemble, we apply the k-medoids cluster analysis as implemented in the *kmedoids* Python library[67] to identify at least two classes of TS geometry for each dehydrogenation step on both surfaces by using the coordination coordinates $C_{N,Fe}$ and $C_{H,Fe}$

III. RESULTS

We study the interaction of an ammonia molecule with the surface, its adsorption, and subsequent cracking at *operando* temperature. The interaction of each intermediate species (NH_2 and NH) with the surface is studied through independent simulations, as well as each dehydrogenation step.

In order to study the reported surface dependence [7–9,11], we study both the dense Fe(110) and the more open Fe(111) at the operando temperature of 700K.

At 700 K on the Fe(110) surface, the surface atomic arrangement is stable, and we do not observe any atomic diffusion. We can anticipate that adsorption sites remain the same as those found in the low-temperature regime, as shown in Fig 1a. That is why we do not report this surface's 300 K behavior, which can be easily deduced from the *operando* temperature results. This is to be contrasted with the highly mobile behavior of the Fe(111) surface atoms as already reported in Ref. 32. This behavior results in continuously forming and destroying surface defects, such as ad-atoms and vacancies. Thus, being the surface behavior rather different from the low temperature one, we also report the 300 K results for comparison. In particular, we find that in addition to the low-temperature absorption sites (Figure 1b), several new ones are available in the *operando* regime, as shown in 1c.

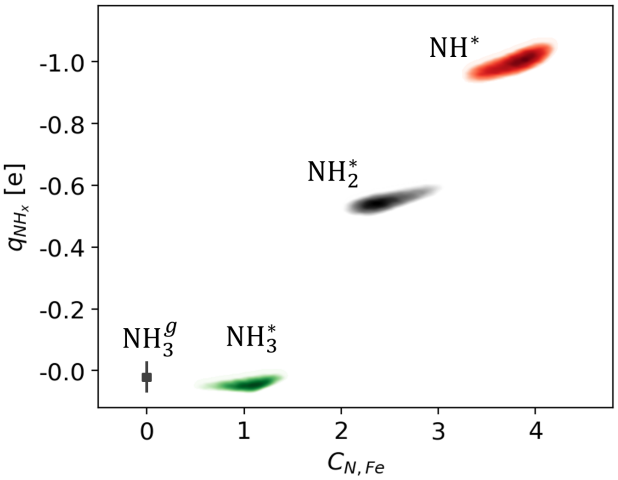

Figure 2. **Interaction of NH_x with Fe(110) surface.** Most stable adsorption sites for the nitrogen hydrides on Fe(110) surface at 700K as a function of the nitrogen-iron coordination number $C_{N,Fe}$ and the total charge transferred from the metallic substrate to the NH_x species q_{NH_x}. Ammonia in both the gas and adsorbed phases is reported. For the adsorbed species, the profiles coincide with the minimum of their FES within the range 0-2 k_BT and are accordingly colored. For NH_3^g, the representation reduces to a point since $C_{N,Fe}$=0 in the gas phase.

A. Interaction between NH_x and iron surfaces

We now discuss the results of simulations of the adsorption and diffusion of the intermediates of the reaction (NH_3, NH_2, and NH) on Fe(110) and Fe(111). In the dynamic approach adopted, adsorption and diffusion are intimately related and describe the catalyst's interaction with the absorbed species. Two-dimensional free energy surfaces (FES) projections are used to explore the coordination numbers, charge transfers, and diffusion pathways.

1. Fe(110)

First, we present the results of the Fe(110). The most energetically stable adsorption configurations of nitrogen hydrides have already been investigated through DFT static calculation; top, short-bridge, and hollow sites have been computed as the minimum energy adsorption sites for NH3, NH2, and NH, respectively[10,16]. At T=0 K, our results are in agreement with the previous theoretical work. In the following, we thus focus on the effects of temperature on this more rigid surface.

In Figure 2, we report the most probable adsorption state obtained from the minimum of free energy surfaces (FES) as a function of the nitrogen-iron coordination number $C_{N,Fe}$, and the total charge transferred from the metallic substrate to the NH_x species q_{NH_x}. This allows characterizing the available adsorption sites, both from geometrical and chemical points of view. In Figure 3, FES are projected along the two in-plane crystallographic directions [001] and [1$\bar{1}$0], from which we can analyze the diffusion mechanism and the related free energy barrier.

NH_3 is preferentially adsorbed on top sites (1-fold coordination). No charge transfers are observed from the substrate to the molecule (Figure 2), However, the ammonia dipole induces a local redistribution of the iron charges, which in a first approximation can be described as a dipole dipole-induced interaction (Figure 3c). This weak bond allows the NH_3 to diffuse easily at 700K through short bridge sites (Figure 3a-b). The computed free energy barrier for diffusing along this pathway is 0.15eV. This diffusion mechanism competes with desorption and subsequent physisorption process.

Contrary to NH_3, NH_2 forms strong chemical bonds with the surface, preferring bridge to top sites. In these 2-fold coordination sites, the metal substrate transfers a charge of -0.6 e to the molecule (Figure 2). Despite its strong chemisorption energy (-3.17 eV[16]), NH_2 is the most mobile surface species. As shown in Figure3a-b amide diffuses between short and long bridge sites through hpc sites (3-fold coordination) with an estimated free energy barrier of 0.05 eV, less than 1 k_BT. So, we can not speak of a single adsorption site due to NH_2 almost barrierless diffusion. The temperature effects play an important role even on these hard surfaces. We can anticipate that the absence of long-lived adsorption states implies a non-negligible increase in the free energy barrier

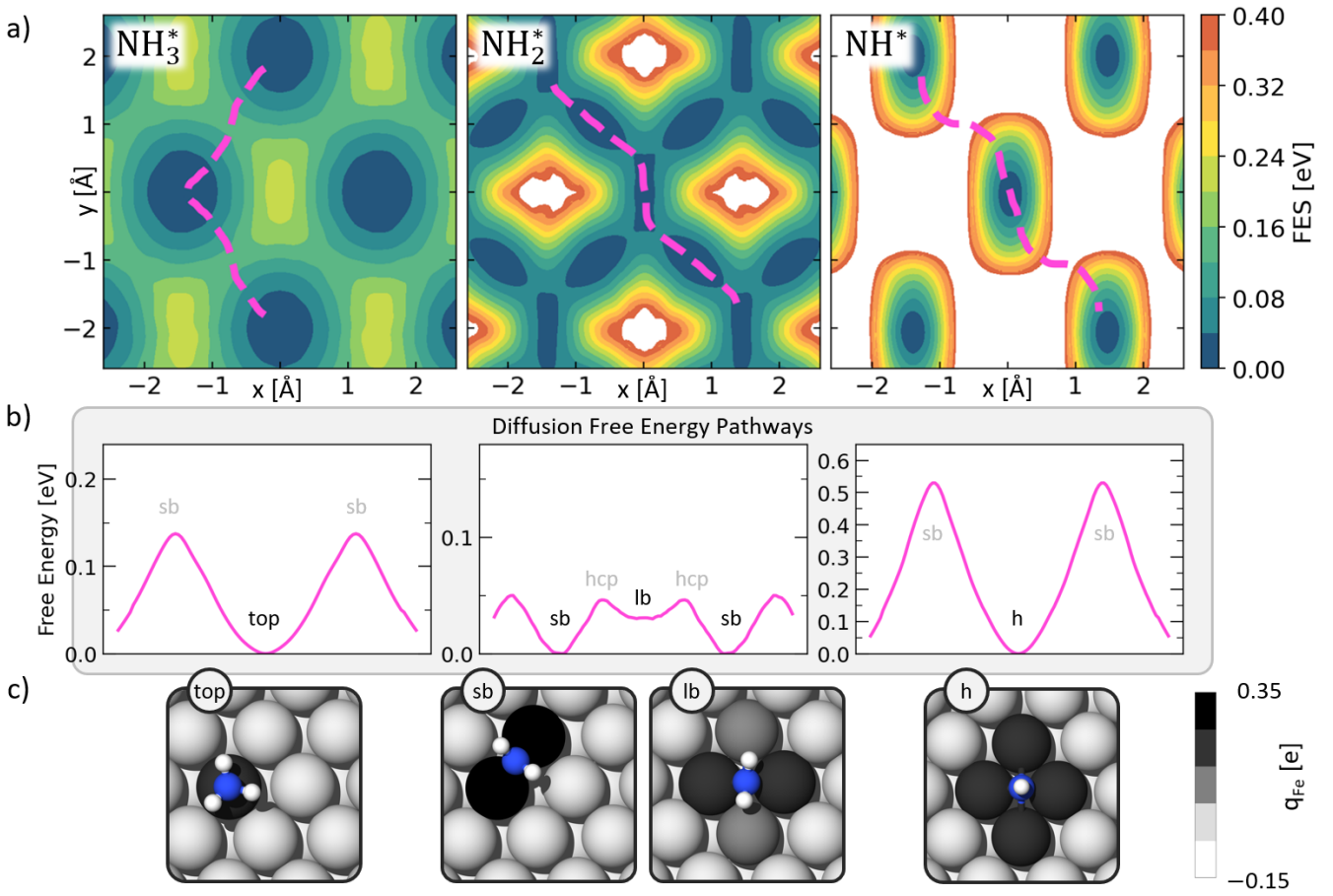

Figure 3. **Diffusion of NH_x^* on Fe(110) surface at 700K.** (a) Free energy of NH_x^* interaction projected along the two crystallographic directions [001] (x-axis) and [1$\bar{1}$0] (y-axis). Local minima represent the metastable states, and fuchsia dashed lines denote the minimum free energy diffusion pathways. (b) Free energy calculated along the minimum free energy pathways. The high symmetry adsorption sites are labeled according to Figure 1. Different scales are used for the free energy to highlight the minima. (c) Snapshots of representative geometries of the minimum free energy adsorption states. Iron atoms are colored according to net charges predicted by the neural network model.

for dehydrogenation.

Finally, NH lives on the hollow sites (4-fold coordination). In this configuration, as shown in Figure 2c, there is a charge transfer of approximately $-1e$ to the molecule, coinciding with an oxidation state of the iron substrate of $+2$. Among the nitrogen hydrides, NH is the less diffusive species. As shown in Figure 3a, imide diffuses between two adjacent hollow sites through a short bridge site. The computed free energy barrier for the diffusion is 0.54 eV (Figure 3b), making the diffusion of NH a rare event. For this species, we can thus speak about long-live adsorption state.

In passing from NH3 to NH, despite the coordination interaction strength increases in terms of charge transfer and coordination (Figure 2), no such relationship with the intermediates' mobility (Figure 3).

2. *Fe(111)*

We now discuss the interaction of nitrogen hydrides with the Fe(111) surface, contrasting, as anticipated, the behavior at T=300K and T=700K. In Figure 4, we show free energy surfaces as a function of the nitrogen-iron coordination number $C_{N,Fe}$, and the total charge transferred q_{NH_x} for each species in the two different temperature regimes. It is important to recall that at T=700K, the surface iron atoms become mobile, forming additional adsorption sites (see Figure 1c). As shown in Figure 4, all the N exhibit a tetrahedral environment due to the chemical drive of N to form an sp_3 hybrid. As a result of surface mobility, this aim can be achieved in different ways in high-temperature regimes. In contrast, at low temperatures, such environments are not accessible. The paradoxical effect of this is to stabilize the adsorption at high temperatures, as indicated by the sharpest minima in the free energy profiles, Figure 4. Such behavior is particularly important for the last two intermediates and

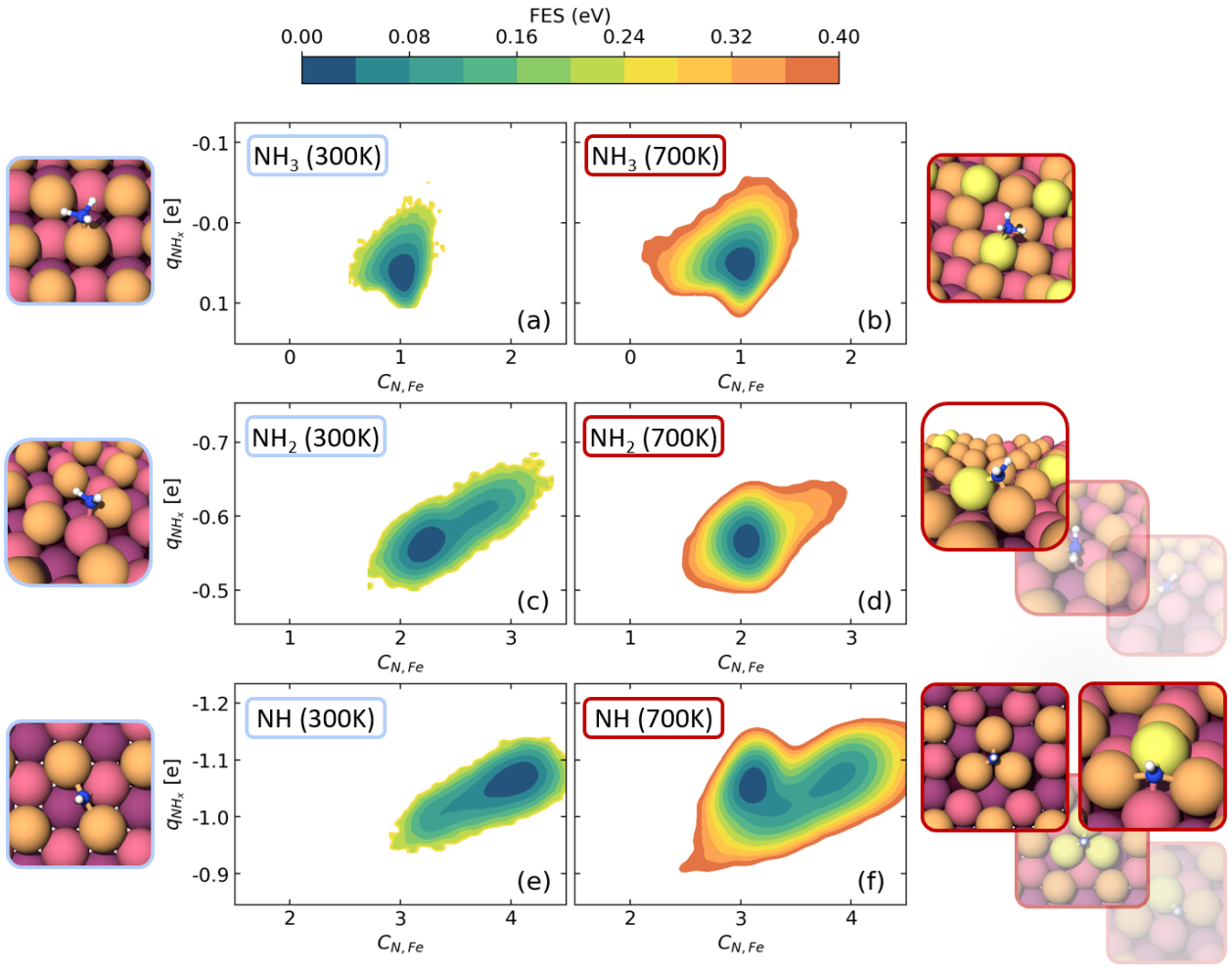

Figure 4. **Interaction of NH_x with Fe(111) surface.** Free energies as a function of the N-Fe coordination and the total charge transferred from the metallic substrate to the NH_x species at T=300 K (a,c,e) and T=700 K (b,d,f). In the snapshots, representative configurations belonging to the adsorption free energy minima are shown.

has significant implications for dehydrogenation, as will be discussed below.

As in Fe(110), NH_3 shows on-top adsorption at low and high temperatures, with no charge transfer. However, unlike Fe(110), NH_3 does not diffuse on the surface. This can be rationalized by considering that the shortest pathway between two on-top sites must go via the lower layers, passing via configurations less favorable than in the gas phase (see Figure 1).

As mentioned above, the adsorption of NH_2 is very different in the two temperature regimes. At T=300K, the amide is bonded in bridge sites between the first and second layers (b12, Figure 1b). In this configuration, NH_2 can move almost barrierless ($\approx$ 0.04eV) between three equivalent b12 bridge sites via the top-layer bridge site (b11, Figure 1b). This behavior is reported in SI Figure S2 and explains the free energy ring minima between the two- and three-fold coordinated state of Figure 4c. At T=700K, these low-temperature adsorption sites are no longer observed, and NH2 is placed only at defective bridge sites (db, Figure 1c). In this configuration, barrierless diffusion of NH_2 is not observed, and the adsorption is stabilized in this two-fold coordinated state.

Finally, we present the interaction of NH with Fe(111), which exhibits significant differences between the high- and low-temperature regimes. At 300K, NH is adsorbed at bridge sites (b11, Figure 1b), while at 700K, a variety of geometrical configurations is observed. The most stable sites for adsorption are the tree-folded coordinated ones (tr1 and tri2, Figure 1c), but also four-fold coordination defective ones are still observed. Despite variations, the iron substrate consistently shares two electrons ($q_{NH} \approx -1e$) with NH, similar to Fe(110).

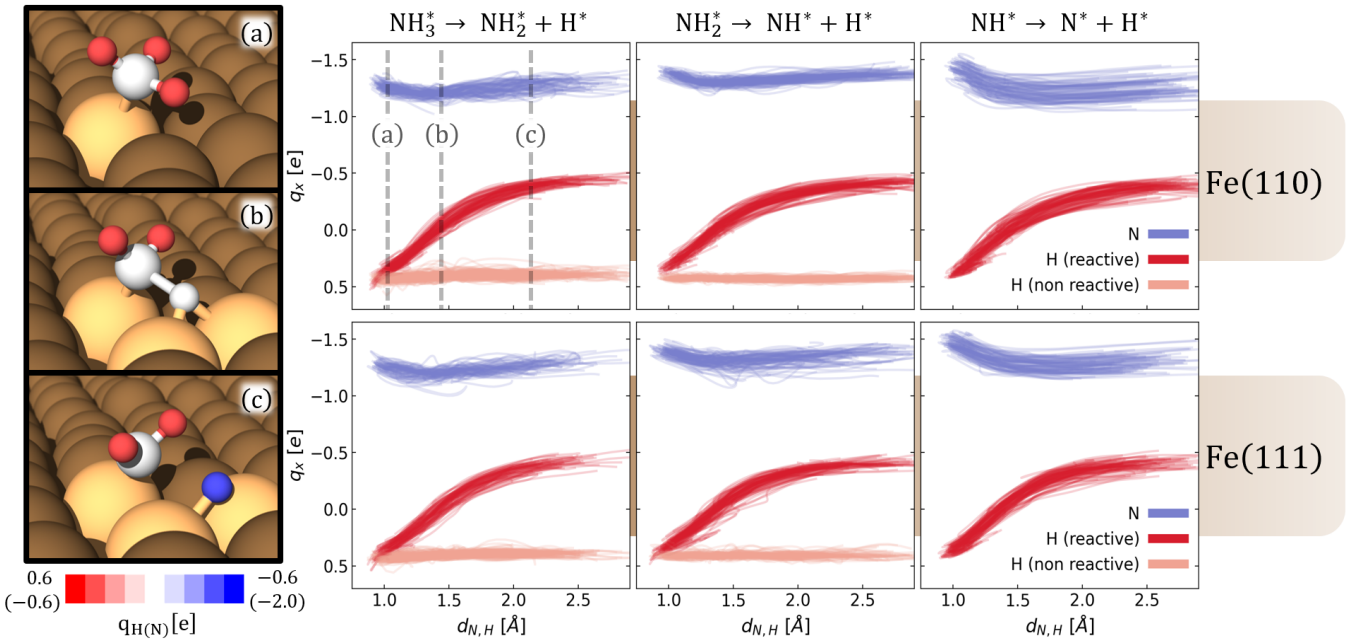

Figure 5. **Dehydrogenation charge variation.** Atoms in the molecule charge variation during reactions as a function of the distance between nitrogen and reactive hydrogen. Each line in the plot (one for each atom) corresponds to a reactive simulation (100 for each event). For each simulation, 40 ps were plotted around the transition state ($d_{N,H} = 1.40$ Å). On the left, we report three snapshots corresponding to the first dehydrogenation step on the Fe(110) surface.

B. Dehydrogenation steps

1. *Reaction mechanism analysis*

As outlined in Section II C 4, one hundred simulations of dehydrogenation events were performed for each step and surface at *operando* temperature, using the OPES-flooding approach. The statistical sampling of reactive pathways was performed without preconceived assumptions about the transition and final states.

A visual inspection revealed a variety of reaction pathways. To get a unified perspective, we use, as in[32], the charge transfer to the nitrogen hydrides to describe the reaction processes. The evolution of the charges in the nitrogen moieties q_x during each dehydrogenation event occurring on both surfaces are plotted in Figure 5. We reasonably assume that the TS is closest to the point where the distance $d_{N,H}$ reaches the breaking point of 1.40 Å (see Section II C 4) and plot the charge variably on a segment of 40 fs centered around the TS.

It can be seen that throughout the reaction, a significant charge variation takes place only to the H atom that is being reduced. This distinctive behavior is exemplified in the left panel of Figure 5, which shows a representative first-step dehydrogenation event on the Fe(110) surface.

When the reactions are studied through these Bader charge lenses, a coherent underlying reaction mechanism becomes evident in spite of the fact that the reaction evolves following different geometrical trajectories. Strikingly, not only is this shared between the individual reactions but also across all the different steps and surfaces.

2. *Transition state ensembles*

We will now describe the observed complexity in TS configurations.

At the *operando* temperature, the adsorbed molecules and the surface atoms exhibit a pronounced mobility that gives each reactive event a distinctive geometric character. Therefore, it is not possible to identify a single transition state (TS); instead, it must be described by an ensemble of structures[68–70]. In SI Figure S3, we report the TS coordinations $C_{N,Fe}$ vs $C_{H,Fe}$ for all reaction steps on the Fe(110) and Fe(111) surfaces. These variables, which provide a coarse geometrical representation of the molecule on the surface during the reaction, exhibit a broad distribution.

Through the application of k-medoids analysis, we identified two clusters within each TS ensemble, as outlined in Section II C 4. The resulting clusters, along with their respective medoids, are depicted in Figure 6 for both Fe(110) and Fe(111) surfaces. In the top panels of Figure 6, we observe for Fe(110) at least two distinguishable classes of geometries, primarily differentiated by $C_{N,Fe}$ for the first and third dehydrogenation steps, and by the coordination number $C_{H,Fe}$ for the second dehydrogenation step. A parallel analysis is conducted for dehydrogenation steps on Fe(111). As depicted in the bottom panels of Figure 6, the first and second TS ensembles are classified based

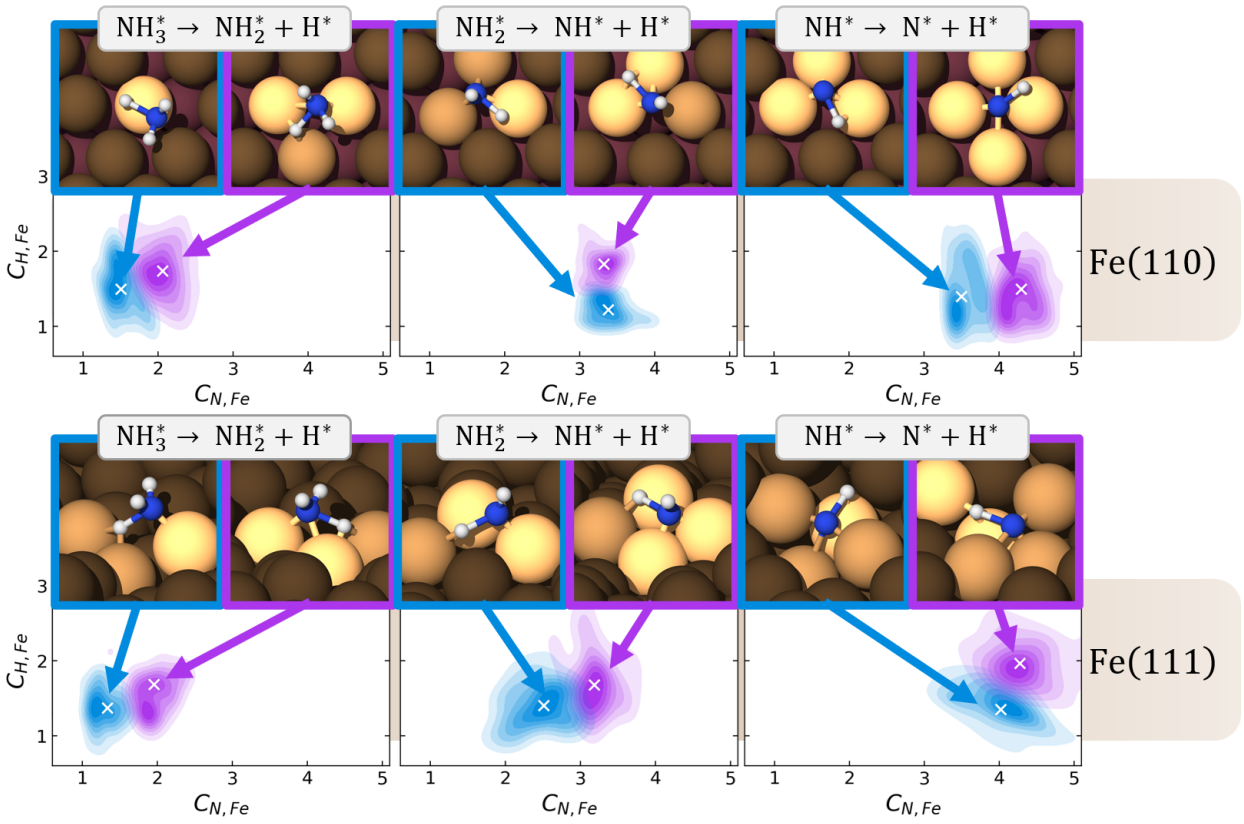

Figure 6. **Transition state ensemble.** Distribution of the coordinations between nitrogen and iron and between reactive hydrogen and iron for the transition state configuration. For each reaction, data are separated in two clusters according to the k-medoids analysis (see Section II C 4). The medoids are indicated with white crosses and shown in the snapshots. Iron atoms are colored to guide the eyes to the difference between clusters: $C_{N,Fe}$ for the second dehydrogenation step on the Fe(110) surface and the last one on the Fe(111) surface; $C_{H,Fe}$ for the others. Row data are reported in SI Figure S3.

on $C_{N,Fe}$, while the third is distinguished by $C_{H,Fe}$. It is noteworthy that the coordination number $C_{N,Fe}$ at the TS consistently exceeds that observed in the most stable adsorption configuration of the reactant (refer to Figs. 2, 4 for Fe(110) and Fe(111), respectively).

The purpose of the above analyses is not to precisely characterize the different TS ensembles but rather to illuminate the great variety of the TS encountered. Thus, we chose to determine only two clusters for each TS ensemble, aimed at obtaining an economical description of such complexity.

Free energy barriers ΔG $[eV]$ at T=700K

	Fe(110)	Fe(111)
$NH_3^* \rightarrow NH_2^* + H^*$	1.01	1.14
$NH_2^* \rightarrow NH^* + H^*$	0.79	1.22
$NH^* \rightarrow N^* + H^*$	1.25	1.10

Table I. **Free energy barrier.** Estimated free energy barrier for each dehydrogenation step on Fe(110) and Fe(111) surface at T=700K. The values are derived from the associated free energy profiles, illustrated in SI Figure S5 and Figure 7, respectively. Considering the accuracy of the ML-potential and the sampling uncertainty of the free energy calculations, we estimated an uncertainty within the range [0.05-0.1] eV.

3. *Dehydrogenation barriers*

In Table I we present the free energy barriers associated with the dehydrogenation steps on both surfaces at the *operando* temperature. The values are obtained from the corresponding free energy profiles, depicted in SI Figure S5 and Figure 7 for Fe(110) and Fe(111), respectively. As described in Section II C 1, our calculations include dynamic aspects, such as the diffusion of adsorbate species and all the possible transition pathways. We point out that the calculated free energy barriers read from the FES at the *operando* temperature differ from the internal energy differences obtained through the static methods (see SI, Figure S6). Dynamical effects are very significant in half of the reactions studied, and in these cases, they cannot be accounted by using the harmonic approximation. Thus, once again[32], the *operando* temperature properties cannot be understood based on the

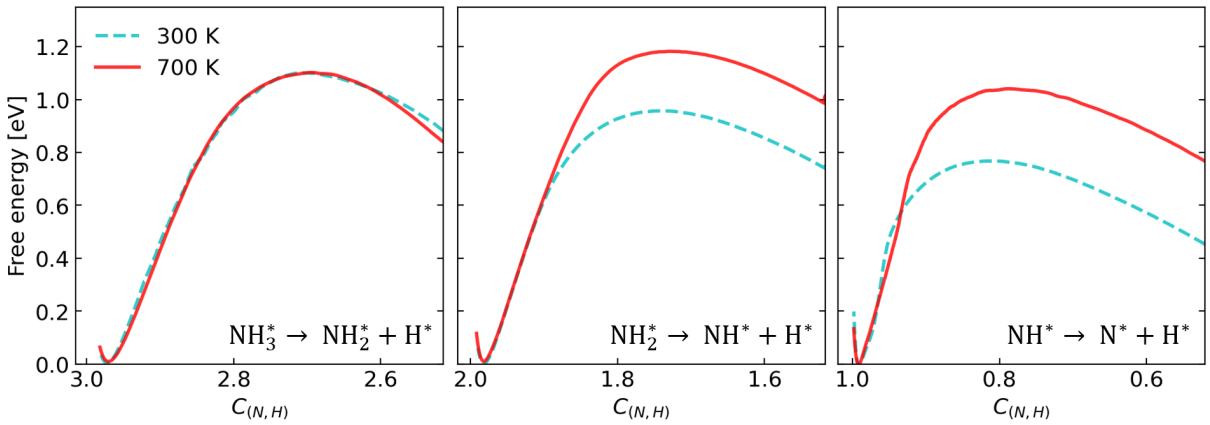

Figure 7. **Fe(111) dehydrogenation barrier.** Free energy profiles of dehydrogenation steps on Fe(111) surface. Blu solid and red dotted lines refer to T=300K and T=700K, respectively. The free energy is projected along the coordination number between nitrogen and hydrogen atoms C_N, H. The free energy of each initial state is set to zero.

low-temperature behavior.

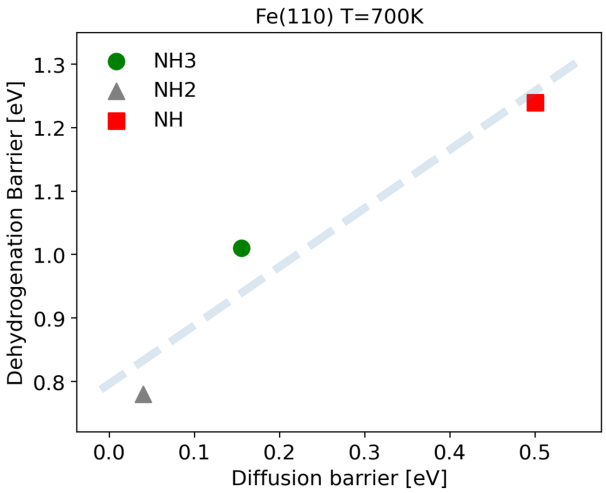

Figure 8. **Correlation between dehydrogenation and diffusion barriers on Fe(110)** Free energy barrier of dehydrogenation steps as a function of the diffusion barrier on Fe(110) surface. All the calculations are performed at the *operando* temperature of 700K. The gray dashed lines follow the linear trend as a guide to the eye.

On Fe(110), the dehydrogenation barriers of various nitrogen hydrides differ significantly, similar to what the diffusion barriers do. Figure 8 shows the clear correlation between these two processes. This is a reflection of the fact that the reduction of one hydrogen atom is driven by the kinetics of NH_x on the surface.

In the case of Fe(111) surface, calculating the diffusion barrier at operando temperature is more complex due to surface dynamical behavior, and we have not attempted to do so. However, the shape of the absorption free energy surfaces (Figure 4) can provide indirect information about the species stability, with broader minima indicating greater dynamism.

If we use this indicator, as well as a visual inspection, we find that NH can perform much longer excursions than NH_3 and NH_2, which have similar behavior (see Figure 4 b,d,f). Thus, also in this case, albeit somewhat indirectly, a correlation between dehydrogenation and diffusion barriers can be observed.

The comparison between T=300K and T=700K is also illuminating. The different adsorption behavior of the nitrogen hydrides, which has been discussed in Section III A 2, is reflected in the dehydrogenation barriers at different temperatures (see Figure 7). Since for NH_3, the adsorption sites and diffusion mechanism are very close at the two temperatures, the two free energy profiles can be almost exactly superimposed. Instead, for NH_2 and NH the 111 surface dynamics forms new, more stable adsorption sites in which the two nitrogen hydrides can be accommodated such that the N atom can have a tetrahedral geometry. This leads to a significant increase in the dehydrogenation barriers.

Consistent with experimental evidence[8], our calculations predict NH as the most stable reaction intermediate on the Fe(110) surface. In the Fe111 case, we observe an interesting change in the rate-limiting step as a function of temperature. At 300K, the most stable intermediate is NH_3. Instead, at 700K, the role of the most intermediate is played by NH_2 in encouraging agreement with the experiments[9].

IV. CONCLUSION

In this study, we have investigated the decomposition of ammonia, and described the adsorption, diffusion, and dehydrogenation of an ammonia molecule on two clean iron surfaces. All through these reaction steps, the effects of dynamics manifest themselves pervasively and in multiple ways.

Even on the (110) surface, which is the most compact

and stable, we saw how the high mobility of the reaction moieties plays a non-negligible role. The effect is even more dramatic for the open (111) surface, where in addition to the intermediates mobility one has to take into account the iron surface atoms diffusivity that, by creating new adsorption sites, significantly alters the free energy profiles.

Analyzing the transition states makes it clear that there is not a single, well-defined one. Still, rather one has to consider an ensemble of transition states. For each dehydrogenation step, there are indeed at least two possible reaction channels. This is the case not only for the more "dynamic" surface (111) but also for the more "static" one (110).

It is important to note how these dynamical effects result in a nontrivial temperature dependence, confirming the gap between the standard approach based on idealized assumption and what happens in the messier *operando* environment.

Molecular dynamics and enhanced sampling techniques, on the other hand, fully account for entropic and dynamic effects, allowing these processes to be studied without any previous assumption. However, it is interesting to note that the same tools that have allowed us to simulate the complex behavior of the system also allow unifying all different dehydrogenation steps on different surfaces using the charge transfer as a descriptor.

Of course, this is a simplified model compared to the actual industrial catalyst, which should require considering the entire catalytic cycle and other effects, such as lateral interactions with adsorbed intermediates and promoter activities. Nevertheless, our study lays the foundation for a principled understanding of the catalytic mechanism of hydrogen extraction from nitrogen hydrides and, consequently, for the rational design of new catalysts.

ACKNOWLEDGMENTS

S.P. is grateful to Umberto Raucci and Enrico Trizio for useful discussions and feedback on the manuscript. We wish to acknowledge the Data Science and Computation Facility and its Support Team at Fondazione Istituto Italiano di Tecnologia, the CINECA award under the ISCRA initiative (IsB26), and the Federal Ministry of Education and Research, Germany (Bundesministerium für Bildung und Forschung, BMBF, Hydrogen flagship project: TransHyDE Forschungsverbund AmmoRef, FKZ 03HY203A) for funding.

REFERENCES

[1]A. Valera-Medina, H. Xiao, M. Owen-Jones, W. I. David, and P. J. Bowen, "Ammonia for power," Progress in Energy and Combustion Science **69**, 63–102 (2018).
[2]C. Zamfirescu and I. Dincer, "Using ammonia as a sustainable fuel," Journal of Power Sources **185**, 459–465 (2008).
[3]A. Klerke, C. H. Christensen, J. K. Nørskov, and T. Vegge, "Ammonia for hydrogen storage: challenges and opportunities," Journal of Materials Chemistry **18**, 2304–2310 (2008).
[4]I. Lucentini, X. Garcia, X. Vendrell, and J. Llorca, "Review of the Decomposition of Ammonia to Generate Hydrogen," (2021).
[5]T. E. Bell and L. Torrente-Murciano, "H2 Production via Ammonia Decomposition Using Non-Noble Metal Catalysts: A Review," Topics in Catalysis 2016 59:15 **59**, 1438–1457 (2016).
[6]N. D. Spencer, R. C. Schoonmaker, and G. A. Somorjai, "Iron single crystals as ammonia synthesis catalysts: Effect of surface structure on catalyst activity," Journal of Catalysis **74**, 129–135 (1982).
[7]G. A. Somorjai and N. Materer, "Surface structures in ammonia synthesis," Topics in Catalysis 1994 1:3 **1**, 215–231 (1994).
[8]M. Weiss, G. Ertl, and F. Nitschke, "ADSORPTION AND DECOMPOSITION OF AMMONIA ON Fe(110)," Applications of Surface Science (1979).
[9]M. Grunze, F. Bozso, G. Ertl, and M. Weiss, "Interaction of ammonia with Fe(111) and Fe(100) surfaces," Applications of Surface Science **1**, 241–265 (1978).
[10]Y. Wang, J. Qian, Z. Fang, M. R. Kunz, G. Yablonsky, A. Fortunelli, W. A. Goddard, and R. R. Fushimi, "Understanding Reaction Networks through Controlled Approach to Equilibrium Experiments Using Transient Methods," Journal of the American Chemical Society **143**, 10998–11006 (2021).
[11]K. Homann, H. Kuhlenbeck, and H. J. Freund, "The interaction of N2 with iron on W(110), Pd(111) and Rh(111)," Zeitschrift fur Physikalische Chemie **198**, 135–147 (1997).
[12]C. M. Goodwin, P. Lömker, D. Degerman, B. Davies, M. Shipilin, F. Garcia-Martinez, S. Koroidov, J. Katja Mathiesen, R. Rameshan, G. L. Rodrigues, C. Schlueter, P. Amann, and A. Nilsson, "Operando probing of the surface chemistry during the Haber–Bosch process," Nature 2024 625:7994 **625**, 282–286 (2024).
[13]S. Satoh, H. Fujimoto, and H. Kobayashi, "Theoretical study of NH3 adsorption on Fe(110) and Fe(111) surfaces," Journal of Physical Chemistry B **110**, 4846–4852 (2006).
[14]R. J. Lin, F. Y. Li, and H. L. Chen, "Computational investigation on adsorption and dissociation of the NH 3 molecule on the Fe(111) surface," Journal of Physical Chemistry C **115**, 521–528 (2011).
[15]G. Lanzani and K. Laasonen, "NH3 adsorption and dissociation on a nanosized iron cluster," International Journal of Hydrogen Energy **35**, 6571–6577 (2010).
[16]X. Duan, J. Ji, G. Qian, C. Fan, Y. Zhu, X. Zhou, D. Chen, and W. Yuan, "Ammonia decomposition on Fe(1 1 0), Co(1 1 1) and Ni(1 1 1) surfaces: A density functional theory study," Journal of Molecular Catalysis A: Chemical **357**, 81–86 (2012).
[17]S. C. Yeo, S. S. Han, and H. M. Lee, "Mechanistic investigation of the catalytic decomposition of ammonia (NH3) on an Fe(100) surface: A DFT study," Journal of Physical Chemistry C **118**, 5309–5316 (2014).
[18]X. Zhang, Z. Lu, D. Ma, and Z. Yang, "Adsorption and dissociation of ammonia on small iron clusters," International Journal of Hydrogen Energy **40**, 346–352 (2015).
[19]L. Xu, D. Kirvassilis, Y. Bai, and M. Mavrikakis, "Atomic and molecular adsorption on Fe(110)," Surface Science **667**, 54–65 (2018).
[20]J. Qian, Q. An, A. Fortunelli, R. J. Nielsen, and W. A. Goddard, "Reaction Mechanism and Kinetics for Ammonia Synthesis on the Fe(111) Surface," Journal of the American Chemical Society **140**, 6288–6297 (2018).
[21]B. Lu, L. Li, M. Ren, Y. Liu, Y. Zhang, X. Xu, X. Wang, and H. Qiu, "Ammonia decomposition over iron-based catalyst: Exploring the hidden active phase," Applied Catalysis B: Environmental **314**, 121475 (2022).
[22]J. Mark, P. Martirez, and E. A. Carter, "First-Principles Insights into the Thermocatalytic Cracking of Ammonia-Hydrogen Blends on Fe(110): 1. Thermodynamics," J. Phys. Chem. C (2022), 10.1021/acs.jpcc.2c06003.
[23]M. S. Spencer, "Stable and metastable metal surfaces in heterogeneous catalysis," Nature 1986 323:6090 **323**, 685–687 (1986).

[24]R. Schlögl, "Heterogeneous Catalysis," Angewandte Chemie International Edition **54**, 3465–3520 (2015).
[25]Y. G. Wang, D. Mei, V. A. Glezakou, J. Li, and R. Rousseau, "Dynamic formation of single-atom catalytic active sites on ceria-supported gold nanoparticles," Nature Communications 2015 6:1 **6**, 1–8 (2015).
[26]L. Grajciar, C. J. Heard, A. A. Bondarenko, M. V. Polynski, J. Meeprasert, E. A. Pidko, and P. Nachtigall, "Towards operando computational modeling in heterogeneous catalysis," Chemical Society Reviews **47**, 8307–8348 (2018).
[27]G. Sun and P. Sautet, "Metastable Structures in Cluster Catalysis from First-Principles: Structural Ensemble in Reaction Conditions and Metastability Triggered Reactivity," Journal of the American Chemical Society **140**, 2812–2820 (2018).
[28]N. Gerrits and G. J. Kroes, "Curious Mechanism of the Dissociative Chemisorption of Ammonia on Ru(0001)," Journal of Physical Chemistry C **123**, 28291–28300 (2019).
[29]W. L. Li, C. N. Lininger, K. Chen, V. Vaissier Welborn, E. Rossomme, A. T. Bell, M. Head-Gordon, and T. Head-Gordon, "Critical Role of Thermal Fluctuations for CO Binding on Electrocatalytic Metal Surfaces," JACS Au **1**, 1708–1718 (2021).
[30]G. Piccini, M. S. Lee, S. F. Yuk, D. Zhang, G. Collinge, L. Kollias, M. T. Nguyen, V. A. Glezakou, and R. Rousseau, "Ab initio molecular dynamics with enhanced sampling in heterogeneous catalysis," Catalysis Science & Technology **12**, 12–37 (2022).
[31]V. Van Speybroeck, M. Bocus, P. Cnudde, and L. Vanduyfhuys, "Operando Modeling of Zeolite-Catalyzed Reactions Using First-Principles Molecular Dynamics Simulations," ACS Catalysis **13**, 11455–11493 (2023).
[32]L. Bonati, D. Polino, C. Pizzolitto, P. Biasi, R. Eckert, S. Reitmeier, R. Schlögl, and M. Parrinello, "The role of dynamics in heterogeneous catalysis: Surface diffusivity and N2 decomposition on Fe(111)," Proceedings of the National Academy of Sciences of the United States of America **120**, e2313023120 (2023).
[33]S. Tripathi, L. Bonati, S. Perego, and M. Parrinello, "How poisoning is avoided in a step of relevance to the Haber-Bosch catalysis," (2023), 10.26434/CHEMRXIV-2023-0ZZCD.
[34]L. Bonati and M. Parrinello, "Silicon Liquid Structure and Crystal Nucleation from Ab Initio Deep Metadynamics," Physical Review Letters **121** (2018), 10.1103/PhysRevLett.121.265701.
[35]H. Niu, L. Bonati, P. M. Piaggi, and M. Parrinello, "Ab initio phase diagram and nucleation of gallium," Nature Communications **11**, 1–9 (2020).
[36]M. Yang, L. Bonati, D. Polino, and M. Parrinello, "Using metadynamics to build neural network potentials for reactive events: the case of urea decomposition in water," Catalysis Today **387**, 143–149 (2022).
[37]M. Yang, U. Raucci, and M. Parrinello, "Reactant-induced dynamics of lithium imide surfaces during the ammonia decomposition process," Nature Catalysis 2023 6:9 **6**, 829–836 (2023).
[38]F. Mambretti, U. Raucci, M. Yang, and M. Parrinello, "How Does Structural Disorder Impact Heterogeneous Catalysts? The Case of Ammonia Decomposition on Non-stoichiometric Lithium Imide," ACS Catalysis **16**, 1252–1256 (2024).
[39]J. Behler and M. Parrinello, "Generalized neural-network representation of high-dimensional potential-energy surfaces," Physical Review Letters **98**, 146401 (2007).
[40]O. T. Unke, S. Chmiela, H. E. Sauceda, M. Gastegger, I. Poltavsky, K. T. Schütt, A. Tkatchenko, and K. R. Müller, "Machine Learning Force Fields," Chemical Reviews (2021), 10.1021/acs.chemrev.0c01111.
[41]L. Zhang, J. Han, H. Wang, and R. Car, "Deep Potential Molecular Dynamics: A Scalable Model with the Accuracy of Quantum Mechanics," Physical Review Letters **120**, 143001 (2018).
[42]L. Zhang, J. Han, H. Wang, W. Saidi, R. Car, and W. E, "End-to-end Symmetry Preserving Inter-atomic Potential Energy Model for Finite and Extended Systems," Advances in Neural Information Processing Systems **31** (2018).
[43]G. Henkelman and H. Jónsson, "A dimer method for finding saddle points on high dimensional potential surfaces using only first derivatives," The Journal of Chemical Physics **111**, 7010–7022 (1999).
[44]J. Kästner and P. Sherwood, "Superlinearly converging dimer method for transition state search," Journal of Chemical Physics **128** (2008), 10.1063/1.2815812/928095.
[45]P. Giannozzi, S. Baroni, N. Bonini, M. Calandra, R. Car, C. Cavazzoni, D. Ceresoli, G. L. Chiarotti, M. Cococcioni, I. Dabo, A. Dal Corso, S. De Gironcoli, S. Fabris, G. Fratesi, R. Gebauer, U. Gerstmann, C. Gougoussis, A. Kokalj, M. Lazzeri, L. Martin-Samos, N. Marzari, F. Mauri, R. Mazzarello, S. Paolini, A. Pasquarello, L. Paulatto, C. Sbraccia, S. Scandolo, G. Sclauzero, A. P. Seitsonen, A. Smogunov, P. Umari, and R. M. Wentzcovitch, "QUANTUM ESPRESSO: a modular and open-source software project for quantum simulations of materials," Journal of Physics: Condensed Matter **21**, 395502 (2009).
[46]P. Giannozzi, O. Andreussi, T. Brumme, O. Bunau, M. Buongiorno Nardelli, M. Calandra, R. Car, C. Cavazzoni, D. Ceresoli, M. Cococcioni, N. Colonna, I. Carnimeo, A. Dal Corso, S. De Gironcoli, P. Delugas, R. A. Distasio, A. Ferretti, A. Floris, G. Fratesi, G. Fugallo, R. Gebauer, U. Gerstmann, F. Giustino, T. Gorni, J. Jia, M. Kawamura, H. Y. Ko, A. Kokalj, E. Kücükbenli, M. Lazzeri, M. Marsili, N. Marzari, F. Mauri, N. L. Nguyen, H. V. Nguyen, A. Otero-De-La-Roza, L. Paulatto, S. Poncé, D. Rocca, R. Sabatini, B. Santra, M. Schlipf, A. P. Seitsonen, A. Smogunov, I. Timrov, T. Thonhauser, P. Umari, N. Vast, X. Wu, and S. Baroni, "Advanced capabilities for materials modelling with Quantum ESPRESSO," Journal of Physics: Condensed Matter **29**, 465901 (2017).
[47]P. Giannozzi, O. Baseggio, P. Bonfà, D. Brunato, R. Car, I. Carnimeo, C. Cavazzoni, S. De Gironcoli, P. Delugas, F. Ferrari Ruffino, A. Ferretti, N. Marzari, I. Timrov, A. Urru, and S. Baroni, "Quantum ESPRESSO toward the exascale," Journal of Chemical Physics **152** (2020), 10.1063/5.0005082/1058748.
[48]J. P. Perdew, K. Burke, and M. Ernzerhof, "Generalized Gradient Approximation Made Simple," Physical Review Letters **77**, 3865 (1996).
[49]A. M. Rappe, K. M. Rabe, E. Kaxiras, and J. D. Joannopoulos, "Optimized pseudopotentials," Physical Review B **41**, 1227 (1990).
[50]N. Marzari, D. Vanderbilt, A. De Vita, and M. C. Payne, "Thermal Contraction and Disordering of the Al(110) Surface," Physical Review Letters **82**, 3296 (1999).
[51]H. J. Monkhorst and J. D. Pack, "Special points for Brillouin-zone integrations," Physical Review B **13**, 5188 (1976).
[52]G. Bussi, D. Donadio, and M. Parrinello, "Canonical sampling through velocity rescaling," Journal of Chemical Physics **126**, 14101 (2007).
[53]R. F. Bader, "Atoms in Molecules," Accounts of Chemical Research **18**, 9–15 (1985).
[54]G. Henkelman, A. Arnaldsson, and H. Jónsson, "A fast and robust algorithm for Bader decomposition of charge density," Computational Materials Science **36**, 354–360 (2006).
[55]K. T. Schütt, H. E. Sauceda, P. J. Kindermans, A. Tkatchenko, and K. R. Müller, "SchNet - A deep learning architecture for molecules and materials," Journal of Chemical Physics **148**, 241722 (2018).
[56]D. P. Kingma and J. L. Ba, "Adam: A Method for Stochastic Optimization," 3rd International Conference on Learning Representations, ICLR 2015 - Conference Track Proceedings (2014).
[57]A. P. Thompson, H. M. Aktulga, R. Berger, D. S. Bolintineanu, W. M. Brown, P. S. Crozier, P. J. in 't Veld, A. Kohlmeyer, S. G. Moore, T. D. Nguyen, R. Shan, M. J. Stevens, J. Tranchida, C. Trott, and S. J. Plimpton, "LAMMPS - a flexible simulation tool for particle-based materials modeling at the atomic, meso, and continuum scales," Computer Physics Communications **271**, 108171 (2022).
[58]J. Zeng, D. Zhang, D. Lu, P. Mo, Z. Li, Y. Chen, M. Rynik, L. Huang, Z. Li, S. Shi, Y. Wang, H. Ye, P. Tuo, J. Yang, Y. Ding, Y. Li, D. Tisi, Q. Zeng, H. Bao, Y. Xia, J. Huang, K. Muraoka, Y. Wang, J. Chang, F. Yuan, S. L. Bore, C. Cai, Y. Lin, B. Wang,

J. Xu, J. X. Zhu, C. Luo, Y. Zhang, R. E. Goodall, W. Liang, A. K. Singh, S. Yao, J. Zhang, R. Wentzcovitch, J. Han, J. Liu, W. Jia, D. M. York, E. Weinan, R. Car, L. Zhang, and H. Wang, "DeePMD-kit v2: A software package for deep potential models," Journal of Chemical Physics **159**, 54801 (2023).

[59] G. A. Tribello, M. Bonomi, D. Branduardi, C. Camilloni, and G. Bussi, "PLUMED 2: New feathers for an old bird," Computer Physics Communications **185**, 604–613 (2014).

[60] M. Invernizzi and M. Parrinello, "Rethinking Metadynamics: From Bias Potentials to Probability Distributions," Journal of Physical Chemistry Letters **11**, 2731–2736 (2020).

[61] M. Invernizzi and M. Parrinello, "Exploration vs Convergence Speed in Adaptive-Bias Enhanced Sampling," Journal of Chemical Theory and Computation **18**, 3988–3996 (2022).

[62] M. Bonomi, G. Bussi, C. Camilloni, G. A. Tribello, P. Banáš, A. Barducci, M. Bernetti, P. G. Bolhuis, S. Bottaro, D. Branduardi, R. Capelli, P. Carloni, M. Ceriotti, A. Cesari, H. Chen, W. Chen, F. Colizzi, S. De, M. De La Pierre, D. Donadio, V. Drobot, B. Ensing, A. L. Ferguson, M. Filizola, J. S. Fraser, H. Fu, P. Gasparotto, F. L. Gervasio, F. Giberti, A. Gil-Ley, T. Giorgino, G. T. Heller, G. M. Hocky, M. Iannuzzi, M. Invernizzi, K. E. Jelfs, A. Jussupow, E. Kirilin, A. Laio, V. Limongelli, K. Lindorff-Larsen, T. Löhr, F. Marinelli, L. Martin-Samos, M. Masetti, R. Meyer, A. Michaelides, C. Molteni, T. Morishita, M. Nava, C. Paissoni, E. Papaleo, M. Parrinello, J. Pfaendtner, P. Piaggi, G. M. Piccini, A. Pietropaolo, F. Pietrucci, S. Pipolo, D. Provasi, D. Quigley, P. Raiteri, S. Raniolo, J. Rydzewski, M. Salvalaglio, G. C. Sosso, V. Spiwok, J. Šponer, D. W. Swenson, P. Tiwary, O. Valsson, M. Vendruscolo, G. A. Voth, and A. White, "Promoting transparency and reproducibility in enhanced molecular simulations," Nature Methods 2019 16:8 **16**, 670–673 (2019).

[63] I. Marcos-Alcalde, E. López-Viñas, and P. Gómez-Puertas, "MEPSAnd: minimum energy path surface analysis over n-dimensional surfaces," Bioinformatics **36**, 956–958 (2020).

[64] A. F. Voter, "A method for accelerating the molecular dynamics simulation of infrequent events," The Journal of Chemical Physics **106**, 4665–4677 (1997).

[65] P. Tiwary and M. Parrinello, "From metadynamics to dynamics," Physical Review Letters **111**, 230602 (2013).

[66] D. Ray, N. Ansari, V. Rizzi, M. Invernizzi, and M. Parrinello, "Rare Event Kinetics from Adaptive Bias Enhanced Sampling," Journal of Chemical Theory and Computation **18**, 6500–6509 (2022).

[67] E. Schubert and L. Lenssen, "Fast k-medoids Clustering in Rust and Python," Journal of Open Source Software **7**, 4183 (2022).

[68] D. Chandler, "Statistical mechanics of isomerization dynamics in liquids and the transition state approximation," The Journal of Chemical Physics **68**, 2959–2970 (1978).

[69] Z. Zhang, B. Zandkarimi, and A. N. Alexandrova, "Ensembles of Metastable States Govern Heterogeneous Catalysis on Dynamic Interfaces," Accounts of Chemical Research **53**, 447–458 (2020).

[70] P. Kang, E. Trizio, M. Parrinello, and A. Simulations, "Computing the Committor with the Committor: an Anatomy of the Transition State Ensemble," (2024).